

# A highly accurate discontinuous Galerkin method for complex interfaces between solids and moving fluids

Martin Käser<sup>1</sup> and Michael Dumbser<sup>2</sup>

## ABSTRACT

We have extended a new highly accurate numerical scheme for unstructured 2D and 3D meshes based on the discontinuous Galerkin approach to simulate seismic wave propagation in heterogeneous media containing fluid-solid interfaces. Because of the formulation of the wave equations as a unified first-order hyperbolic system in velocity stress, the fluid can be in movement along the interface. The governing equations within the moving fluid are derived from well-known first principles in fluid mechanics. The discontinuous Galerkin approach allows for jumps of the material parameters and the solution across element interfaces, which are handled by Riemann solvers or numerical fluxes. The use of Riemann solvers at the element interfaces makes the treatment of the fluid particularly simple by setting the shear

modulus in the fluid region to zero. No additional compatibility relations, such as vanishing shear stress or continuity of normal stresses, are necessary to couple the solid and fluid along an interface. The Riemann solver automatically recognizes the jump of the material coefficients at the interface and provides the correct numerical fluxes for fluid-solid contacts. Therefore, wave propagation in the entire computational domain containing heterogeneous media, namely moving fluids and elastic solids, can be described by a uniform set of acoustic and elastic wave equations. The accuracy of the proposed scheme is confirmed by comparing numerical results against analytic solutions. The potential of the new method was demonstrated in a 3D model problem typical for marine seismic exploration with a fluid-solid interface determined by a complicated bathymetry.

## INTRODUCTION

Numerical modeling has become an increasingly important tool not only in global seismology but also in seismic exploration. Nowadays, the comparisons of real measurements from seismic data acquisition in the field with synthetic data are invaluable in the investigation of the complete 3D seismic wavefield generated by, e.g., a complex reservoir structure, free surface, or bathymetry. For classical numerical methods, e.g., the finite-difference (FD) method, it is still a challenging task to model correctly the interface waves arising at contacts between different materials or waves created by surface topography (e.g., Robertsson, 1996; Moczo et al., 2007b).

In particular, interfaces between fluids and solid materials can cause numerical artifacts (e.g., Kiefling and Feng, 1976). At a fluid-solid interface, the physical boundary condition is represented by perfect slip; i.e., the shear stress has to vanish, whereas the continuity of the normal stress and velocities has to be guaranteed. Furthermore, standard FD schemes present accuracy problems at sharp ma-

terial discontinuities, as shown, e.g., by Cunha (1993) and Zahradník et al. (1993), particularly if there is no alignment with the grid (van Vossen et al., 2002). However, Moczo et al. (2002, 2007a) report recent improvements of the FD method.

In the context of the finite-element method, different approaches to avoid purely numerical problems at fluid-solid interfaces were introduced (e.g., Zienkiewicz and Bettess, 1978; Bermudez et al., 1999). These approaches use displacement in the solid material and pressure in the fluid. Thompson (1994) has shown that a velocity potential can be used in the fluid leading to a symmetric discrete system of equations, which exhibits a block-diagonal mass matrix. However, the density of the fluid must be homogeneous.

In the framework of the spectral-element (SE) method, Komatitsch et al. (2000) extended this approach so that the discretization results in a global mass matrix that is exactly diagonal by construction. The advantage over classical FE methods (e.g., Seriani et al., 1992; Priolo et al., 1994) lies in the enhanced efficiency on parallel

Manuscript received by the Editor 14 May 2007; revised manuscript received 22 October 2007; published online 19 March 2008.

<sup>1</sup>Ludwig-Maximilians-Universität München, Department für Geo- und Umweltwissenschaften, Geophysik, München, Germany. E-mail: kaeser@geophysik.lmu.de.

<sup>2</sup>Universität Stuttgart, Institut für Aerodynamik und Gasdynamik, Stuttgart, Germany. E-mail: iagmidu@iag.uni-stuttgart.de.

© 2008 Society of Exploration Geophysicists. All rights reserved.

computers because no inversion of large linear systems is necessary. Chaljub et al. (2003) successfully applied the SE method on a fluid-solid heterogeneous sphere.

Recently, Zhang (2004) introduced a grid-method (GM) approach for heterogeneous media with high velocity contrasts. He extended his approach to the problem of fluid-solid interfaces with complex geometry. However, he also must use two approaches for treating the displacements in the elastic regions and the pressure in the acoustic regions. Furthermore, an explicit interface condition has to be specified for the integral approach. In addition, a quite fine mesh spacing is required to achieve accurate results.

In particular, the interface between a fluid and an elastic solid is of major importance in marine exploration seismology. Fluid-solid contacts typically generate an interface wave, the Scholte wave (Scholte, 1942), that is trapped near this fluid-solid interface. Today, generated Scholte waves often are used in marine geophysics to estimate shallow shear-wave-velocity structures of marine sediments down to 100 m or more beneath the seafloor (Kawashima and Kimura, 1998). The perfect slip condition between the fluid and the solid requires the shear stress to vanish at the interface to avoid the entrance of shear stress waves in the fluid. This is handled in a way similar to what is known from the free-surface boundary condition. Most numerical methods typically must handle fluid-solid interfaces with care. Special treatment is required, e.g., arithmetic averaging of effective medium parameters, for FD methods (van Vossen et al., 2002), predictor-multicorrector staggered-time schemes for SE methods (Komatitsch et al., 2000), or particular integral equations to fulfill the interface boundary conditions in the GM method (Zhang, 2004).

We present an extension of a new numerical approach to the problem of fluid-solid interfaces, based on the highly accurate discontinuous Galerkin (DG) method combined with a time-integration method using arbitrary high-order derivatives (ADER) recently introduced in numerical seismology (de la Puente et al., 2007; Dumbser and Käser, 2006; Dumbser et al., 2007; Käser and Dumbser, 2006; Käser et al., 2007). The seismic wave equation is solved in the velocity-stress formulation expressed as a first-order hyperbolic system of partial differential equations. The unknowns are approximated with piecewise polynomials inside each element, where discontinuities are allowed at element interfaces.

Because of the use of an exact Riemann solver to compute numerical fluxes across element interfaces, no special treatment of fluid-solid interfaces is necessary even if the fluid is moving. The Riemann solver automatically recognizes discontinuities in the material parameters. The computational mesh (triangular or tetrahedral) is aligned with the fluid-solid interface by using commercial software for computer-aided design and mesh generation. The acoustic fluid can be characterized simply by setting its shear modulus  $\mu$  to zero.

Furthermore, the fluid does not have to be at rest but can move with time. The fluid velocity can vary throughout the fluid. Therefore, effects of ocean currents for deep-ocean simulations can be determined with high accuracy. We remark that the wave-propagation process in a moving fluid can be treated only by expressing the wave equation as a first-order hyperbolic system, e.g., in the velocity-stress formulation, because the physical effect of convection leads to a first-order differential operator.

The paper is arranged as follows. First we derive the governing equations based on fundamental principles of fluid mechanics leading to a hyperbolic system that describes acoustic wave propagation in fluids as well as elastic wave propagation in solids. Next we

present the main ingredients of the new extended numerical scheme to handle a moving fluid and show the stability condition restricting the time step. Finally, we validate our results by comparisons with analytic solutions before applying the new ADER-DG scheme to a 3D test case with complex bathymetry including vertical segments of the seafloor.

## GOVERNING EQUATIONS

Here, we derive the partial differential equations describing the wave propagation in an elastic solid and an acoustic fluid. To arrive at such a comprehensive formulation of a unified system of governing equations, we formally combine the classical velocity-stress formulation for wave propagation in elastic solids with the acoustic wave equations derived from fluid dynamics, including the case of a moving fluid.

First we present the classical velocity-stress formulation for wave propagation in a resting, purely elastic medium that is well known in the field of seismology. Without showing the details of the standard derivation from Hooke's law, the definition of strains, and the dynamic relationship between the acceleration and net force resulting from the stresses (see LeVeque, 2002), the equations for stresses and velocities without source terms are

$$\begin{aligned}
 \frac{\partial}{\partial t} \sigma_{xx} - (\lambda + 2\mu) \frac{\partial}{\partial x} u' - \lambda \frac{\partial}{\partial y} v' - \lambda \frac{\partial}{\partial z} w' &= 0, \\
 \frac{\partial}{\partial t} \sigma_{yy} - \lambda \frac{\partial}{\partial x} u' - (\lambda + 2\mu) \frac{\partial}{\partial y} v' - \lambda \frac{\partial}{\partial z} w' &= 0, \\
 \frac{\partial}{\partial t} \sigma_{zz} - \lambda \frac{\partial}{\partial x} u' - \lambda \frac{\partial}{\partial y} v' - (\lambda + 2\mu) \frac{\partial}{\partial z} w' &= 0, \\
 \frac{\partial}{\partial t} \sigma_{xy} - \mu \left( \frac{\partial}{\partial x} v' + \frac{\partial}{\partial y} u' \right) &= 0, \\
 \frac{\partial}{\partial t} \sigma_{yz} - \mu \left( \frac{\partial}{\partial z} v' + \frac{\partial}{\partial y} w' \right) &= 0, \\
 \frac{\partial}{\partial t} \sigma_{xz} - \mu \left( \frac{\partial}{\partial z} u' + \frac{\partial}{\partial x} w' \right) &= 0, \\
 \rho \frac{\partial}{\partial t} u' - \frac{\partial}{\partial x} \sigma_{xx} - \frac{\partial}{\partial y} \sigma_{xy} - \frac{\partial}{\partial z} \sigma_{xz} &= 0, \\
 \rho \frac{\partial}{\partial t} v' - \frac{\partial}{\partial x} \sigma_{xy} - \frac{\partial}{\partial y} \sigma_{yy} - \frac{\partial}{\partial z} \sigma_{yz} &= 0, \\
 \rho \frac{\partial}{\partial t} w' - \frac{\partial}{\partial x} \sigma_{xz} - \frac{\partial}{\partial y} \sigma_{yz} - \frac{\partial}{\partial z} \sigma_{zz} &= 0. \quad (1)
 \end{aligned}$$

Here, as usual, the normal stresses are indicated by  $\sigma_{xx}$ ,  $\sigma_{yy}$ ,  $\sigma_{zz}$ ; the shear stresses by  $\sigma_{xy}$ ,  $\sigma_{yz}$ ,  $\sigma_{xz}$ ; and the components of the particle velocities by  $u'$ ,  $v'$ ,  $w'$ .

The following is a brief review of the standard derivation of the acoustic wave equations from the fundamental equations of fluid dynamics (e.g., Hirsch, 1990; Landau and Lifshitz, 1959) given by the conservation of mass and momentum of the form

$$\frac{\partial \rho}{\partial t} + \nabla \cdot (\rho \mathbf{v}) = \frac{\partial \rho}{\partial t} + \mathbf{v} \cdot \nabla \rho + \rho \nabla \cdot \mathbf{v} = 0, \quad (2)$$

$$\frac{\partial \mathbf{v}}{\partial t} + (\mathbf{v} \cdot \nabla) \mathbf{v} + \frac{\nabla p}{\rho} = 0, \quad (3)$$

where  $\rho$  denotes mass density,  $\mathbf{v} = (u, v, w)$  fluid velocity, and  $p$  pressure.

Linear acoustic wave propagation then is derived by assuming small density, velocity, and pressure perturbation of a background state; i.e., we can introduce the decompositions

$$\rho = \rho_0 + \rho', \quad \mathbf{v} = \mathbf{v}_0 + \mathbf{v}' \quad \text{and} \quad p = p_0 + p', \quad (4)$$

where the density, velocity, and pressure fields associated with the background flow are denoted as  $\rho_0$ ,  $\mathbf{v}_0 = (u_0, v_0, w_0)$  and  $p_0$ , respectively, and the density, velocity, and pressure fluctuations in the fluid are represented by  $\rho'$ ,  $\mathbf{v}' = (u', v', w')$  and  $p'$ . For linear acoustic wave propagation, the density and pressure fluctuations are small with respect to the background state, i.e.,  $\rho' \ll \rho_0$  and  $p' \ll p_0$ .

Furthermore, for the case of most liquids, we can assume that the background fluid is inviscid ( $\mu = 0$ ) and incompressible, i.e.,  $\rho_0 = \text{const}$  in space and time. Note that the background flow itself is not calculated but is specified as an input function of time and space. This assumption, along with the fact that the background flow  $\mathbf{v}_0$  itself obeys the conservation of mass (equation 2), provides the classical divergence-free condition for the background velocity field

$$\nabla \cdot \mathbf{v}_0 = 0. \quad (5)$$

The previous assumptions are justified for linear acoustic waves in inviscid and incompressible fluids and in particular for most liquids. Based on these assumptions, we first derive the governing partial differential equation for the pressure perturbation  $p'$ . Toward this end, we insert the perturbation ansatz (equation 4), the incompressibility assumption, and the divergence-free property (equation 5) of the background flow into the equation of mass conservation (equation 2). Note that in the linear case, the quantities of the fluctuations are so small that their products can be ignored (LeVeque, 2002), which yields the following expression for the density perturbation:

$$\frac{\partial \rho'}{\partial t} + \mathbf{v}_0 \cdot \nabla \rho' + \rho_0 \nabla \cdot \mathbf{v}' = 0. \quad (6)$$

According to Landau and Lifshitz (1959), isentropic pressure perturbations  $p'$  can be linked to the density fluctuations  $\rho'$  by the equation of state,

$$p' = c_p^2 \rho', \quad (7)$$

where  $c_p$  denotes the acoustic wave speed, and is defined, as usual, in terms of density  $\rho$  and bulk modulus  $K$  as

$$c_p^2 = \frac{K}{\rho} = \frac{\lambda}{\rho}, \quad (8)$$

because for an inviscid fluid, the shear modulus is  $\mu = 0$ , and hence  $K = \lambda$ . Using equation 4 in the definition (equation 8), neglecting  $\rho'$  against  $\rho_0$ , and inserting it along with equation 7 into equation 6, leads to the final equation for the pressure perturbation  $p'$  of the form

$$\frac{\partial p'}{\partial t} + \mathbf{v}_0 \cdot \nabla p' + \lambda \nabla \cdot \mathbf{v}' = 0. \quad (9)$$

Furthermore, the well-known relation between the pressure and the stress tensor in fluid mechanics (e.g., Hirsch, 1990; Landau and Lifshitz, 1959) is given by

$$\boldsymbol{\sigma} = -p' \mathbf{I} + \boldsymbol{\tau}, \quad (10)$$

where for the inviscid fluids, the shear stress  $\boldsymbol{\tau}$  vanishes, i.e.,  $\boldsymbol{\tau} = 0$ . Note that here,  $\mathbf{I}$  denotes the unit matrix. Therefore, in fluids, the normal stresses are identical to the negative pressure fluctuations, i.e.,  $\sigma_{xx} = \sigma_{yy} = \sigma_{zz} = -p'$ .

In addition, we need the governing partial differential equation for the velocity fluctuations  $\mathbf{v}'$ . Again, we use the perturbation ansatz (equation 4) but insert it into the conservation of momentum (equation 3) and obtain

$$\begin{aligned} \frac{\partial \mathbf{v}_0}{\partial t} + \frac{\partial \mathbf{v}'}{\partial t} + ((\mathbf{v}_0 + \mathbf{v}') \cdot \nabla)(\mathbf{v}_0 + \mathbf{v}') \\ + \frac{\nabla p_0 + \nabla p'}{\rho_0 + \rho'} = 0. \end{aligned} \quad (11)$$

Using the property in equation 5 and the fact that the background flow  $\mathbf{v}_0$  itself obeys equation 3 and again linearizing the equation by neglecting  $\rho'$  against  $\rho_0$  and the products of small fluctuations, we get the final equation for the velocity perturbation  $\mathbf{v}'$  of the form

$$\frac{\partial \mathbf{v}'}{\partial t} + (\mathbf{v}_0 \cdot \nabla) \mathbf{v}' + \frac{\nabla p'}{\rho_0} = -(\mathbf{v}' \cdot \nabla) \mathbf{v}_0. \quad (12)$$

Equations 9 and 12 are the governing equations for linear acoustic wave propagation in incompressible moving fluids and usually are called the linearized Euler equations (see Bogey et al., 2002). Note that the movement of the fluid is included in both equations via the background flow  $\mathbf{v}_0$  and that for very small fluctuations  $\mathbf{v}'$  or spatially nearly constant background flow  $\mathbf{v}_0$ , the source term  $(\mathbf{v}' \cdot \nabla) \mathbf{v}_0$  in equation 12 can be omitted. For a generalization of these equations to more general weakly compressible fluids with variable density and temperature, see Munz et al. (2007).

The use of equation 10 to express the acoustic equations 9 and 12 similarly to the velocity-stress formulation (equation 1) leads to the equation system

$$\begin{aligned} \frac{\partial}{\partial t} \sigma_{xx} + u_0 \frac{\partial}{\partial x} \sigma_{xx} + v_0 \frac{\partial}{\partial y} \sigma_{xx} + w_0 \frac{\partial}{\partial z} \sigma_{xx} \\ - \lambda \left( \frac{\partial}{\partial x} u' + \frac{\partial}{\partial y} v' + \frac{\partial}{\partial z} w' \right) = 0, \\ \frac{\partial}{\partial t} \sigma_{yy} + u_0 \frac{\partial}{\partial x} \sigma_{yy} + v_0 \frac{\partial}{\partial y} \sigma_{yy} + w_0 \frac{\partial}{\partial z} \sigma_{yy} \\ - \lambda \left( \frac{\partial}{\partial x} u' + \frac{\partial}{\partial y} v' + \frac{\partial}{\partial z} w' \right) = 0, \\ \frac{\partial}{\partial t} \sigma_{zz} + u_0 \frac{\partial}{\partial x} \sigma_{zz} + v_0 \frac{\partial}{\partial y} \sigma_{zz} + w_0 \frac{\partial}{\partial z} \sigma_{zz} \\ - \lambda \left( \frac{\partial}{\partial x} u' + \frac{\partial}{\partial y} v' + \frac{\partial}{\partial z} w' \right) = 0, \\ \frac{\partial}{\partial t} u' + u_0 \frac{\partial}{\partial x} u' + v_0 \frac{\partial}{\partial y} u' + w_0 \frac{\partial}{\partial z} u' - \frac{1}{\rho_0} \frac{\partial}{\partial x} \sigma_{xx} \end{aligned}$$

$$\begin{aligned}
&= -u' \frac{\partial}{\partial x} u_0 - v' \frac{\partial}{\partial y} u_0 - w' \frac{\partial}{\partial z} u_0, \\
\frac{\partial}{\partial t} v' + u_0 \frac{\partial}{\partial x} v' + v_0 \frac{\partial}{\partial y} v' + w_0 \frac{\partial}{\partial z} v' - \frac{1}{\rho_0} \frac{\partial}{\partial y} \sigma_{yy} \\
&= -u' \frac{\partial}{\partial x} v_0 - v' \frac{\partial}{\partial y} v_0 - w' \frac{\partial}{\partial z} v_0, \\
\frac{\partial}{\partial t} w' + u_0 \frac{\partial}{\partial x} w' + v_0 \frac{\partial}{\partial y} w' + w_0 \frac{\partial}{\partial z} w' - \frac{1}{\rho_0} \frac{\partial}{\partial z} \sigma_{zz} \\
&= -u' \frac{\partial}{\partial x} w_0 - v' \frac{\partial}{\partial y} w_0 - w' \frac{\partial}{\partial z} w_0, \tag{13}
\end{aligned}$$

which describes the wave propagation in an acoustic medium with background flow  $\mathbf{v}_0$ . Note that here, the first three equations are identical because, in the acoustic case, all normal stresses are equal and represent the pressure variations  $p'$ . However, we separate them to show clearly the analogy to the elastic equations.

Finally, we can combine the equation systems 1 and 13 and formally express them as a unified linear hyperbolic system leading to the combined 3D wave equations for the elastic solids and acoustic liquids with background flow  $\mathbf{v}_0$  in the form

$$\begin{aligned}
&\frac{\partial}{\partial t} \sigma_{xx} + u_0 \frac{\partial}{\partial x} \sigma_{xx} + v_0 \frac{\partial}{\partial y} \sigma_{xx} + w_0 \frac{\partial}{\partial z} \sigma_{xx} \\
&\quad - (\lambda + 2\mu) \frac{\partial}{\partial x} u' - \lambda \frac{\partial}{\partial y} v' - \lambda \frac{\partial}{\partial z} w' = 0, \\
&\frac{\partial}{\partial t} \sigma_{yy} + u_0 \frac{\partial}{\partial x} \sigma_{yy} + v_0 \frac{\partial}{\partial y} \sigma_{yy} + w_0 \frac{\partial}{\partial z} \sigma_{yy} \\
&\quad - \lambda \frac{\partial}{\partial x} u' - (\lambda + 2\mu) \frac{\partial}{\partial y} v' - \lambda \frac{\partial}{\partial z} w' = 0, \\
&\frac{\partial}{\partial t} \sigma_{zz} + u_0 \frac{\partial}{\partial x} \sigma_{zz} + v_0 \frac{\partial}{\partial y} \sigma_{zz} + w_0 \frac{\partial}{\partial z} \sigma_{zz} \\
&\quad - \lambda \frac{\partial}{\partial x} u' - \lambda \frac{\partial}{\partial y} v' - (\lambda + 2\mu) \frac{\partial}{\partial z} w' = 0, \\
&\frac{\partial}{\partial t} \sigma_{xy} + u_0 \frac{\partial}{\partial x} \sigma_{xy} + v_0 \frac{\partial}{\partial y} \sigma_{xy} + w_0 \frac{\partial}{\partial z} \sigma_{xy} \\
&\quad - \mu \left( \frac{\partial}{\partial x} v' + \frac{\partial}{\partial y} u' \right) = 0, \\
&\frac{\partial}{\partial t} \sigma_{yz} + u_0 \frac{\partial}{\partial x} \sigma_{yz} + v_0 \frac{\partial}{\partial y} \sigma_{yz} + w_0 \frac{\partial}{\partial z} \sigma_{yz} \\
&\quad - \mu \left( \frac{\partial}{\partial z} v' + \frac{\partial}{\partial y} w' \right) = 0, \\
&\frac{\partial}{\partial t} \sigma_{xz} + u_0 \frac{\partial}{\partial x} \sigma_{xz} + v_0 \frac{\partial}{\partial y} \sigma_{xz} + w_0 \frac{\partial}{\partial z} \sigma_{xz} \\
&\quad - \mu \left( \frac{\partial}{\partial z} u' + \frac{\partial}{\partial x} w' \right) = 0,
\end{aligned}$$

$$\begin{aligned}
&\frac{\partial}{\partial t} u' + u_0 \frac{\partial}{\partial x} u' + v_0 \frac{\partial}{\partial y} u' + w_0 \frac{\partial}{\partial z} u' \\
&\quad - \frac{1}{\rho_0} \left( \frac{\partial}{\partial x} \sigma_{xx} + \frac{\partial}{\partial y} \sigma_{xy} + \frac{\partial}{\partial z} \sigma_{xz} \right) \\
&= -u' \frac{\partial}{\partial x} u_0 - v' \frac{\partial}{\partial y} u_0 - w' \frac{\partial}{\partial z} u_0, \\
&\frac{\partial}{\partial t} v' + u_0 \frac{\partial}{\partial x} v' + v_0 \frac{\partial}{\partial y} v' + w_0 \frac{\partial}{\partial z} v' \\
&\quad - \frac{1}{\rho_0} \left( \frac{\partial}{\partial x} \sigma_{xy} + \frac{\partial}{\partial y} \sigma_{yy} + \frac{\partial}{\partial z} \sigma_{yz} \right) \\
&= -u' \frac{\partial}{\partial x} v_0 - v' \frac{\partial}{\partial y} v_0 - w' \frac{\partial}{\partial z} v_0, \\
&\frac{\partial}{\partial t} w' + u_0 \frac{\partial}{\partial x} w' + v_0 \frac{\partial}{\partial y} w' + w_0 \frac{\partial}{\partial z} w' \\
&\quad - \frac{1}{\rho_0} \left( \frac{\partial}{\partial x} \sigma_{xz} + \frac{\partial}{\partial y} \sigma_{yz} + \frac{\partial}{\partial z} \sigma_{zz} \right) \\
&= -u' \frac{\partial}{\partial x} w_0 - v' \frac{\partial}{\partial y} w_0 - w' \frac{\partial}{\partial z} w_0. \tag{14}
\end{aligned}$$

We emphasize that the acoustic part of the combined system (equation 14) is valid only for a divergence-free, incompressible, inviscid ( $\mu = 0$ ) fluid moving with  $\mathbf{v}_0 = \mathbf{v}_0(x, y, z, t)$ . Note that the purely acoustic case is retrieved from equation 14 when setting the shear modulus  $\mu$  and the initial condition of the shear stresses to zero (equation 14). In this case, the governing equations 9 and 12 derived from fluid mechanics are retrieved.

Within the solid, there is, of course, no background flow, and hence  $\mathbf{v}_0 = 0$ . In this case, the unified equation 14 system reduces to the classical system of the elastic wave equations (equation 1). We emphasize that the formulation of the combined equations (equation 14) represents the key enabler that allows our new numerical scheme to treat jointly the acoustic and elastic cases. In this way, the algorithm can deal with both media merely by choosing the corresponding physically relevant material parameters. No additional interface conditions are needed to couple the acoustic medium and the elastic medium.

The main purpose for the formally combined wave equations (equation 14) is to allow us to apply a single numerical scheme using new Jacobian matrices that depend on the material properties assigned to each element. This also explains why we formally keep the second, third, and fourth terms in equations 3–5 in equation 14 which, in fact, are always zero. Note that in the elastic case,  $\mathbf{v}_0 = 0$ , whereas in the acoustic case,  $\sigma_{xy} = \sigma_{yz} = \sigma_{xz} = 0$ . The correct coupling then is achieved automatically by the exact Riemann solver described below in equation 19. Note, however, that the mesh must conform to any fluid-solid discontinuity; i.e., the element interfaces must be aligned with such a material interface.

## THE NUMERICAL SCHEME

The 3D wave equation in the velocity-stress formulation (equation 14) can be written in a compact form as a first-order hyperbolic system of partial differential equations of the form

$$\frac{\partial \mathbf{Q}_p}{\partial t} + \mathbf{A}_{pq} \frac{\partial \mathbf{Q}_q}{\partial x} + \mathbf{B}_{pq} \frac{\partial \mathbf{Q}_q}{\partial y} + \mathbf{C}_{pq} \frac{\partial \mathbf{Q}_q}{\partial z} = \mathbf{E}_{pq} \mathbf{Q}_q + \mathbf{s}_p, \quad (15)$$

where  $\mathbf{Q}$  is the vector of the nine unknown variables indexed by  $p$ , i.e., the stresses and velocities such that  $\mathbf{Q} = (\sigma_{xx}, \sigma_{yy}, \sigma_{zz}, \sigma_{xy}, \sigma_{yz}, \sigma_{xz}, u', v', w')^T$ . Note that classical tensor notation is used, which implies summation over each index that appears twice. The matrices  $\mathbf{A}_{pq}$ ,  $\mathbf{B}_{pq}$ , and  $\mathbf{C}_{pq}$  are the space-dependent Jacobian matrices, and  $\mathbf{E}_{pq}$  is the matrix describing a reactive source term. All matrices are of size  $9 \times 9$ , where  $p$  identifies the row and  $q$  the column. The vector  $\mathbf{s}_p$  is an external source term.

In the ADER-DG approach, a 2D or 3D computational domain  $\Omega$  is divided into conforming triangular or tetrahedral elements  $T^{(m)}$  being addressed by a unique index  $(m)$ . In the following, we briefly give the 3D formulation, which can be reduced simply to the 2D case by ignoring the last term of the left-hand side of equation 15 and reducing the size of the Jacobians to  $5 \times 5$ , because we have only  $\mathbf{Q} = (\sigma_{xx}, \sigma_{yy}, \sigma_{xy}, u', v')^T$  (Käser and Dumbser, 2006).

The numerical solution  $\mathbf{Q}_h$  of equation 15 is approximated inside each element  $T^{(m)}$  by a linear combination of space-dependent polynomial basis functions  $\Phi_l(\xi, \eta, \zeta)$  of degree  $N$  and time-dependent degrees of freedom  $\hat{\mathbf{Q}}_{pl}^{(m)}(t)$ ,

$$(\mathbf{Q}_h^{(m)})_p(\xi, \eta, \zeta, t) = \hat{\mathbf{Q}}_{pl}^{(m)}(t) \Phi_l(\xi, \eta, \zeta), \quad (16)$$

where  $\xi$ ,  $\eta$ , and  $\zeta$  are the coordinates in a canonical reference element  $T_E$  (Dumbser and Käser, 2006). The index  $h$  denotes the numerical solution, the index  $p$  stands for the number of unknowns in the vector  $\mathbf{Q}$ , and  $l$  indicates the  $l$ th basis function. The explicit form of the basis functions  $\Phi_l(\xi, \eta, \zeta)$  is shown in Appendix A.

Note that the index  $l$  ranges from 0 to its maximum value  $L - 1$ , where  $L = \frac{1}{2}(N+1)(N+2)$  or  $L = \frac{1}{6}(N+1)(N+2)(N+3)$  are the numbers of required basis functions in 2D and 3D, respectively, depending on the polynomial degree  $N$ . Furthermore, we remark that a polynomial degree  $N$  leads to a numerical approximation order of  $N + 1$ .

Multiplying equation 15 by a test function  $\Phi_k$  and integrating over an element  $T^{(m)}$  gives

$$\int_{T^{(m)}} \Phi_k \frac{\partial \mathbf{Q}_p}{\partial t} dV + \int_{T^{(m)}} \Phi_k \left( \mathbf{A}_{pq} \frac{\partial \mathbf{Q}_q}{\partial x} + \mathbf{B}_{pq} \frac{\partial \mathbf{Q}_q}{\partial y} + \mathbf{C}_{pq} \frac{\partial \mathbf{Q}_q}{\partial z} \right) dV = \int_{T^{(m)}} \Phi_k (\mathbf{E}_{pq} \mathbf{Q}_q + \mathbf{s}_p) dV. \quad (17)$$

Integration of equation 17 by parts then yields

$$\begin{aligned} & \int_{T^{(m)}} \Phi_k \frac{\partial \mathbf{Q}_p}{\partial t} dV + \int_{\partial T^{(m)}} \Phi_k \mathbf{F}_p^h dS - \int_{T^{(m)}} \left( \frac{\partial \Phi_k}{\partial x} \mathbf{A}_{pq} \right. \\ & \quad \left. + \frac{\partial \Phi_k}{\partial y} \mathbf{B}_{pq} + \frac{\partial \Phi_k}{\partial z} \mathbf{C}_{pq} \right) \mathbf{Q}_q dV \\ & = \int_{T^{(m)}} \Phi_k (\mathbf{E}_{pq} \mathbf{Q}_q + \mathbf{s}_p) dV, \end{aligned} \quad (18)$$

where a numerical flux  $\mathbf{F}_p^h$  has been introduced in the surface integral because  $\mathbf{Q}_h$  might be discontinuous at an element boundary in the DG approach.

For a detailed derivation of the fully discrete formulation of the ADER-DG scheme, the reader is referred to the introductory papers by Käser and Dumbser (2006) and by Dumbser and Käser (2006). There, the flux  $\mathbf{F}_p^h$  is derived for a coordinate system, which is aligned with the outward-pointing unit normal vector  $\mathbf{n}$  of an element boundary, i.e., an edge of a triangle in the 2D case or a triangular face of a tetrahedron in the 3D case. The required transformation of the unknowns in vector  $\mathbf{Q}_p$  from the global Cartesian system to the locally normal, edge- or face-aligned coordinate system is given by the rotation matrix  $(\mathbf{T}_{pq})^{-1}$  (Käser and Dumbser, 2006; Dumbser and Käser, 2006).

## Numerical flux

For the linear system given by equation 15, we use an exact Riemann solver to compute the flux across element interfaces by up-winding. For a detailed description of Riemann solvers, see the textbooks of Toro (1999) and LeVeque (2002). The flux is computed using only the Jacobian matrix  $\mathbf{A}_{pq}$  in the  $x$ -direction with the material properties of the local element. Therefore, in the global Cartesian  $xyz$ -system, the numerical flux  $\mathbf{F}_p^h$  in equation 18 for element  $T^{(m)}$  across the interface with one of the neighbor elements  $T^{(j)}$  is given as

$$\begin{aligned} \mathbf{F}_p^h = & \frac{1}{2} \mathbf{T}_{pq} ((\mathbf{A}_{qr}^n)^{(m)} + |\mathbf{A}_{qr}^n|^{(m)}) (\mathbf{T}_{rs})^{-1} \hat{\mathbf{Q}}_{sl}^{(m)} \Phi_l^{(m)} \\ & + \frac{1}{2} \mathbf{T}_{pq} ((\mathbf{A}_{qr}^n)^{(m)} - |\mathbf{A}_{qr}^n|^{(m)}) (\mathbf{T}_{rs})^{-1} \hat{\mathbf{Q}}_{sl}^{(j)} \Phi_l^{(m_j)}, \end{aligned} \quad (19)$$

where  $\hat{\mathbf{Q}}_{sl}^{(m)} \Phi_l^{(m)}$  and  $\hat{\mathbf{Q}}_{sl}^{(j)} \Phi_l^{(m_j)}$  are the boundary extrapolated values of the numerical solution from element  $T^{(m)}$  and the  $j$ th side neighbor  $T^{(j)}$ , respectively.

For the 2D case, we have  $j = 1, \dots, 3$ ; for the 3D case, we have  $j = 1, \dots, 4$ . The Jacobian matrix  $(\mathbf{A}_{qr}^n)^{(m)}$  contains the material parameters of element  $T^{(m)}$  aligned with the *normal* direction  $\mathbf{n} = (n_x, n_y, n_z)^T$  to the  $j$ th side of the element. The matrix  $\mathbf{T}_{pq}$  represents the back-transformation into the global  $xyz$ -system. We point out that the boundary-extrapolated values of both elements adjacent to an interface contribute to the numerical flux. Note that the numerical flux respects the nonconservative form of the governing equation 15.

In the following, we give the explicit form of  $(\mathbf{A}_{qr}^n)^{(m)}$  and the absolute value  $|\mathbf{A}_{qr}^n|^{(m)}$  of the Jacobian matrix necessary to compute the numerical flux. We do not distinguish the cases of a moving fluid or a fluid at rest, because the fluid at rest represents only the special case of a moving fluid with flow velocity  $\mathbf{v}_0 = 0$ . The notation  $|\mathbf{A}_{qr}^n|^{(m)}$  of the absolute value of the Jacobian matrix has the meaning of applying the absolute value operator to its eigenvalues  $a_1, a_2, \dots$ , i.e.,

$$\begin{aligned} |\mathbf{A}_{qr}^n|^{(m)} &= \mathbf{R}_{qp}^n |\mathbf{A}_{ps}| (\mathbf{R}_{sr}^n)^{-1}, \text{ with} \\ |\mathbf{A}_{ps}| &= \text{diag}(|a_1|, |a_2|, \dots), \end{aligned} \quad (20)$$

where  $\mathbf{R}_{qp}^n$  is the matrix of the right eigenvectors of  $\mathbf{A}_{qr}^n$ .

As shown by the formally unified equations (equation 14), for the case of a background convection with local convection speed  $\mathbf{v}_0 = (u_0, v_0, w_0)^T$ , the combined system matrices must be modified with respect to the standard elastic wave equations (Käser and Dumbser, 2006; Dumbser and Käser, 2006) by simply adding the normal con-



vection speed  $u_n = \mathbf{n} \cdot \mathbf{v}_0$  to the diagonal of the matrices  $\mathbf{A}_{pq}^n$ . The eigenvectors  $\mathbf{R}_{qp}^n$  remain unchanged by this modification, whereas all eigenvalues  $a_1, a_2, \dots$  are modified by adding the value of the normal velocity  $u_n$ .

The resulting matrices  $\mathbf{A}_{pq}^n$  and  $|\mathbf{A}_{pq}^n|$  for computing the flux in the normal direction  $\mathbf{n}$  are

$$\mathbf{A}_{pq}^n = \begin{pmatrix} u_n & 0 & 0 & 0 & 0 & 0 & -\rho_0 c_p^2 & 0 & 0 \\ 0 & u_n & 0 & 0 & 0 & 0 & -\lambda & 0 & 0 \\ 0 & 0 & u_n & 0 & 0 & 0 & -\lambda & 0 & 0 \\ 0 & 0 & 0 & u_n & 0 & 0 & 0 & -\mu & 0 \\ 0 & 0 & 0 & 0 & u_n & 0 & 0 & 0 & 0 \\ 0 & 0 & 0 & 0 & 0 & u_n & 0 & 0 & -\mu \\ -\frac{1}{\rho_0} & 0 & 0 & 0 & 0 & 0 & u_n & 0 & 0 \\ 0 & 0 & 0 & -\frac{1}{\rho_0} & 0 & 0 & 0 & u_n & 0 \\ 0 & 0 & 0 & 0 & 0 & -\frac{1}{\rho_0} & 0 & 0 & u_n \end{pmatrix}, \quad (21)$$

$$|\mathbf{A}_{pq}^n| = \begin{pmatrix} \alpha_p & 0 & 0 & 0 & 0 & 0 & 0 & 0 & 0 \\ \frac{\lambda}{\rho_0 c_p} & |u_n| & 0 & 0 & 0 & 0 & 0 & 0 & 0 \\ \frac{\lambda}{\rho_0 c_p} & 0 & |u_n| & 0 & 0 & 0 & 0 & 0 & 0 \\ 0 & 0 & 0 & \alpha_s & 0 & 0 & 0 & 0 & 0 \\ 0 & 0 & 0 & 0 & \alpha_s & 0 & 0 & 0 & 0 \\ 0 & 0 & 0 & 0 & 0 & \alpha_s & 0 & 0 & 0 \\ 0 & 0 & 0 & 0 & 0 & 0 & \alpha_p & 0 & 0 \\ 0 & 0 & 0 & 0 & 0 & 0 & 0 & \alpha_s & 0 \\ 0 & 0 & 0 & 0 & 0 & 0 & 0 & 0 & \alpha_s \end{pmatrix},$$

with  $c_p = \sqrt{\lambda + 2\mu/\rho_0}$  and  $c_s = \sqrt{\mu/\rho_0}$  being the P- and S-wave velocities of the material and  $\alpha_p = c_p + |u_n|$  and  $\alpha_s = c_s + |u_n|$  the absolute values of the modified eigenvalues. We remark that the matrices for the case of a solid are obtained simply by setting  $u_n = 0$  and those for a fluid by setting  $\mu = 0$ .

The final form of the fully discrete ADER-DG scheme reads as follows:

$$\begin{aligned} & [(\hat{\mathbf{Q}}_{pl}^{(m)})^{n+1} - (\hat{\mathbf{Q}}_{pl}^{(m)})^n] |J| \mathbf{M}_{kl} + \frac{1}{2} \sum_{j=1}^4 \mathbf{T}_{pq}^j ((\mathbf{A}_{qr}^n)^{(m)}) \\ & + |\mathbf{A}_{qr}^n|^{(m)} (\mathbf{T}_{rs}^j)^{-1} |S_j| \mathbf{F}_{kl}^{-j} \cdot \mathbf{I}_{slmn}(\Delta t) (\hat{\mathbf{Q}}_{mn}^{(m)})^n \\ & + \frac{1}{2} \sum_{j=1}^4 \mathbf{T}_{pq}^j ((\mathbf{A}_{qr}^n)^{(m)} - |\mathbf{A}_{qr}^n|^{(m)}) \\ & \times (\mathbf{T}_{rs}^j)^{-1} |S_j| \mathbf{F}_{kl}^{+j,i,h} \cdot \mathbf{I}_{slmn}(\Delta t) (\hat{\mathbf{Q}}_{mn}^{(m_j)})^n \end{aligned}$$

$$\begin{aligned} & - \mathbf{A}_{pq}^* |J| \mathbf{K}_{kl}^\xi \cdot \mathbf{I}_{qlmn}(\Delta t) (\hat{\mathbf{Q}}_{mn}^{(m)})^n - \mathbf{B}_{pq}^* |J| \mathbf{K}_{kl}^\eta \cdot \mathbf{I}_{qlmn}(\Delta t) \\ & \times (\hat{\mathbf{Q}}_{mn}^{(m)})^n - \mathbf{C}_{pq}^* |J| \mathbf{K}_{kl}^\zeta \cdot \mathbf{I}_{qlmn}(\Delta t) (\hat{\mathbf{Q}}_{mn}^{(m)})^n \\ & = \mathbf{E}_{pq} \cdot \mathbf{I}_{qlmn}(\Delta t) (\hat{\mathbf{Q}}_{mn}^{(m)})^n |J| \mathbf{M}_{kl} + \int_n^{n+1} \int_{T_E} \Phi_k s_p dV. \quad (22) \end{aligned}$$

Here,  $\mathbf{M}_{kl}$  denotes the elementary mass matrix;  $\mathbf{K}_{kl}^\xi$ ,  $\mathbf{K}_{kl}^\eta$ , and  $\mathbf{K}_{kl}^\zeta$  are the elementary stiffness matrices; and  $\mathbf{F}_{kl}^{-j}$  and  $\mathbf{F}_{kl}^{+j,i,h}$  are the elementary flux matrices. The DG formulation causes all of these matrices to be elementary matrices because the coupling between the elements is achieved via the numerical flux.

Because of the introduction of a reference element, all mass, stiffness, and flux matrices must be computed only once on the reference element. The tensor  $\mathbf{I}_{qlmn}(\Delta t)$  denotes the time integration via the Cauchy-Kovalevski procedure, and  $|J|$  is the determinant of the Jacobian matrix of the transformation from the physical tetrahedron  $T^{(m)}$  into the reference tetrahedron  $T_E$ . The size of the  $j$ th face of the tetrahedron  $T^{(m)}$  is denoted by  $|S_j|$ . More details can be found in Dumbser and Käser (2006).

## STABILITY CONDITION

The stability of our explicit time-stepping scheme is controlled by the stability number introduced by Courant et al. (1928), often called the CFL number. For a thorough investigation of the linear stability properties of the ADER-DG schemes via a von Neumann analysis, see Dumbser (2005). Dumbser shows that the stability limit for the ADER-DG scheme is slightly lower than that for Runge-Kutta DG schemes.

Therefore, the CFL number is set in all our computations to 50% of the stability limit  $1/(2N + 1)$  of the Runge-Kutta DG schemes, resulting in the stability limit for our time step given by

$$\Delta t < \frac{1}{2N + 1} \cdot \min_{(m)} \frac{r^{(m)}}{a^{(m)}}, \quad (23)$$

where  $r^{(m)}$  is the radius of the incircle or insphere of a triangular or tetrahedral element  $T^{(m)}$ , respectively, and  $a^{(m)}$  is the maximum signal speed, i.e., the maximum eigenvalue of the Jacobians  $\mathbf{A}_{pq}^n$ , arising in this element. As shown in the previous section, in the case of the moving fluid, this signal speed is given by the sum of the P-wave propagation velocity and the normal fluid's convection speed  $u_n^{(m)}$ , so that  $a^{(m)} = c_p^{(m)} + u_n^{(m)}$ .

## VALIDATION

A classical 2D test case to validate the implementation of fluid-solid interfaces consists of two homogeneous half-spaces, i.e., an acoustic material and an elastic material in contact at a plane interface. The solution for a compressional point source and a plane interface can be computed analytically (e.g., Pilant, 1979) and hence can be used to evaluate numerical results. For this paper, we use the FORTRAN code EX2DELEL of Berg et al. (1994) to compute the analytic solutions. The code EX2DELEL is based on the Cagniard de Hoop technique (de Hoop, 1960; de Hoop and van der Hijden, 1983), which allows for the use of an arbitrary-source time function for displacements or velocities.

The setup of the physical problem is similar to that of Komatitsch et al. (2000), who used the SE method (Komatitsch and Vilotte, 1998; Komatitsch and Tromp, 1999). The computational domain is  $\Omega = [-4000 \text{ m}, 4000 \text{ m}] \times [-3000 \text{ m}, 3000 \text{ m}]$ , with an acoustic medium ( $z > 0$ ) over an elastic medium ( $z < 0$ ) separated by a plane fluid-solid interface at  $z = 0$ . The material parameters of the two media are given in Table 1. The domain  $\Omega$  is discretized by 43,184 triangular elements of an average edge length of 50 m. The minimum occurring edge length is 29 m in the solid material, and the minimum radius of incircles  $r^{(m)}$  is 8 m, which affects the stability criterion and therefore determines the maximum possible time step, as given in equation 23.

The domain boundaries are absorbing boundaries; see Käser and Dumbser (2006) and Dumbser and Käser (2006) for details. The source is a compressional point source with a Ricker wavelet as source time function

$$S(t) = a_1(0.5 + a_2(t - t_D)^2)e^{a_2(t - t_D)^2}, \quad (24)$$

where  $t_D = 115 \text{ ms}$  is the source delay time and  $a_1 = 1 \times 10^{14}$  and  $a_2 = -(\pi f_c)^2$  are constants determining the amplitude and frequency of the Ricker wavelet of central frequency  $f_c = 10 \text{ Hz}$ . Therefore, the exact expression of the resulting source vector  $\mathbf{s}_p$  acting on the governing partial differential equation 15 is

$$\mathbf{s}_p(\mathbf{x}, t) = (1, 1, 0, 0, 0)^T \cdot \frac{S(t)}{\rho_0(\mathbf{x})} \cdot \delta(\mathbf{x} - \mathbf{x}_s), \quad (25)$$

where  $\mathbf{x}_s = (x_s, z_s)$  is the point-source location.

For the following numerical experiments, we use an ADER-DG O3 and an ADER-DG O6 scheme; the first scheme provides an accuracy in space and time of order three and the second scheme an accuracy in space and time of order six. For the order three case, the time step is  $5.8 \times 10^{-4} \text{ s}$ , and for the order six case, it is  $2.1 \times 10^{-4} \text{ s}$ . The final simulation time is 3.0 s. For comparison, we run the lower-order ADER-DG O3 scheme on a refined mesh of 172,992 triangles with an average edge length of 25 m, which leads to a time step of  $2.9 \times 10^{-4} \text{ s}$ .

### Source and receiver in the acoustic medium

In the first numerical experiment, the source is located at  $\mathbf{x}_s = (x_s, z_s) = (0, -500) \text{ m}$ , and a receiver is positioned at  $\mathbf{x}_r = (x_r, z_r) = (2177.3, -533.33) \text{ m}$ , i.e., both above the fluid-solid interface. We remark that neither the source nor the receiver locations must coincide with a mesh vertex. Through the definition of the approximation function in equation 16, each element contains the continuous information of high-order polynomials that can be evaluated exactly at any point location inside the element (Käser and Dumbser, 2006).

**Table 1. Material parameters for the test cases of a fluid-solid interface between an acoustic medium and an elastic medium.**

	$c_p$ (m/s)	$c_s$ (m/s)	$\rho_0$ (kg/m <sup>3</sup> )	$\lambda$ (GPa)	$\mu$ (GPa)
Acoustic	1500	0.000	1020	2.295	0.000
Elastic	3400	1963	2500	9.633	9.633

A snapshot of the normal stress component  $\sigma_{xx}$  is plotted at time  $t = 1.25 \text{ s}$  in Figure 1 (top) for the case of the fluid at rest obtained with the ADER-DG O6 scheme. The locations of the source and receiver are indicated with an empty and a full circle, respectively. The (a) direct and (b) reflected acoustic pressure waves are clearly visible in the fluid. In the solid, we see the (c) transmitted P-wave with longer wavelength caused by the higher velocity and (d) the converted P-to-S-wave (d).

In addition, a symmetric pattern of refracted head waves (e) and (f) generated along the fluid-solid interface can be observed, as in the experiment of Komatitsch et al. (2000). The Scholte wave (g) is hardly visible at the triple point where the direct P-wave and the reflected P-wave in the fluid meet the converted P-to-S-wave in the solid. This is because of the small velocity contrast of the acoustic P-wave (a) and the elastic S-wave (d) that have not yet separated sufficiently after  $t = 1.25 \text{ s}$ .

In Figure 2a and b, we compare the analytic solution and the different numerical solutions of the horizontal and vertical velocity components of the wavefield at receiver location  $\mathbf{x}_r$ . The agreement of all phases is excellent, confirming the high accuracy of the ADER-DG O6 scheme, even on the coarse unstructured triangulations with a mesh spacing of  $h = 50 \text{ m}$ . The results of the ADER-DG O3 scheme on the same mesh show insufficient accuracy. On the refined

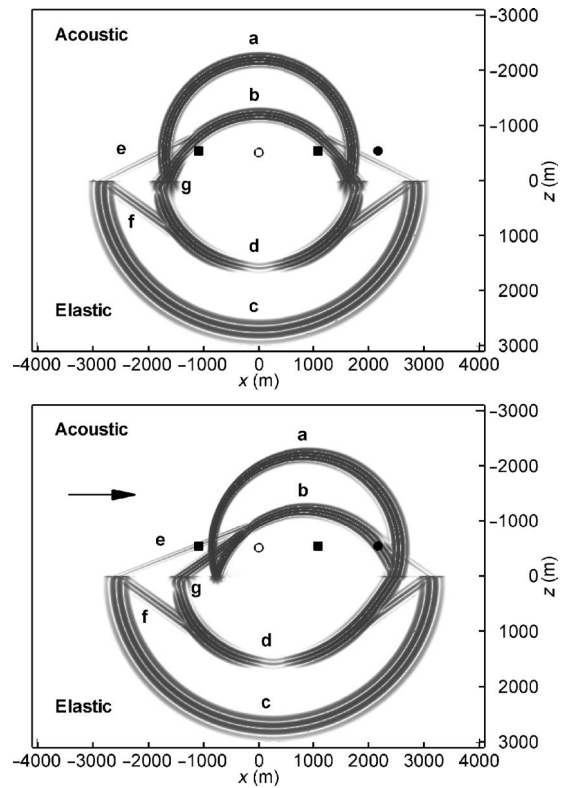


**Figure 1.** Snapshot of the stress component  $\sigma_{xx}$  at  $t = 1.25 \text{ s}$  with (top) the fluid at rest and (bottom) the fluid moving with 750 m/s to the right. Different wave phases show a deformation caused by the moving fluid as well as asymmetrically distorted wave patterns. The source position is indicated by the white circle. Receiver positions are indicated by the black circle and squares. Indications for different wave types are: (a) the direct wave, (b) the reflected acoustic pressure waves, (c) the transmitted P-wave, (d) the converted P-to-S-wave, (e) and (f) the refracted head waves, and (g) the Scholte wave.

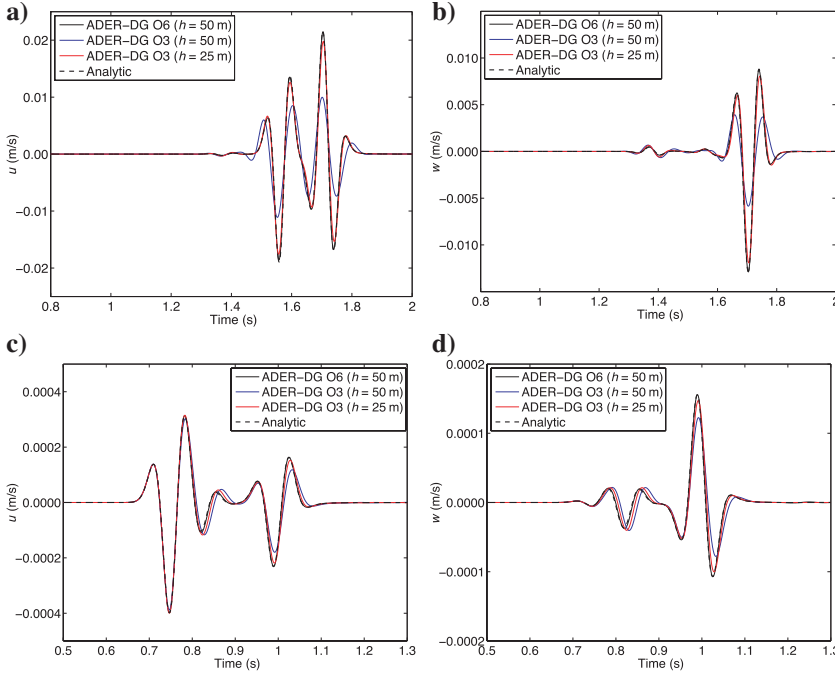


Figure 2. Comparison of numerical and analytic seismograms for the resting fluid. Parts (a) and (b) show the results for the case of the source and receiver in the acoustic medium obtained by the ADER-DG O6 scheme and the ADER-DG O3 scheme on the 50-m mesh and the ADER-DG O3 scheme on a refined 25-m mesh. Parts (c) and (d) show the results for the case of the source and receiver in the elastic medium obtained by the ADER-DG O6 scheme and the ADER-DG O3 scheme on the 50-m mesh and the ADER-DG O3 scheme on a refined 25-m mesh.

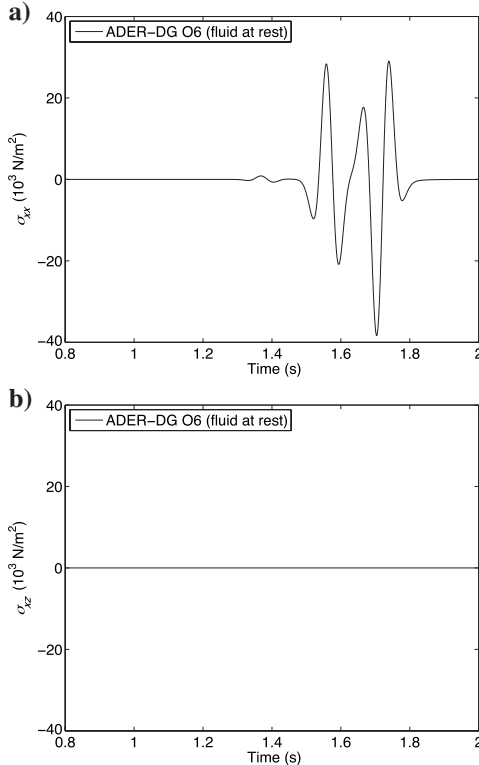


Figure 3. Seismograms for the case of the source and receiver in the acoustic medium: The numerical solution of (a) the normal stress component  $\sigma_{xx}$  and (b) the shear stress component  $\sigma_{xz}$  obtained with the ADER-DG O6 scheme for the case with the fluid at rest.

mesh with  $h = 25$  m, the results of the ADER-DG O3 clearly improve. However, the results remain worse than those for the ADER-DG O6 scheme on the coarse mesh.

The computational time on a SGI Altix 4700 platform using eight Intel Itanium2 Madison processors, each with 1.6 GHz and 4 GByte of RAM, was 1036 s for the ADER-DG O3 scheme on the coarse mesh. In comparison, the simulation with the ADER-DG O6 scheme took 9450 s, whereas the ADER-DG O3 simulation on the fine mesh took 7740 s. Therefore, we can confirm the results of previous work (Dumbser and Käser, 2006) claiming that higher-order schemes on coarse meshes pay off compared with lower-order schemes on fine meshes. Furthermore, in Figure 3, we show the numerical results of ADER-DG O6 simulation for the normal and shear stress components  $\sigma_{xx}$  and  $\sigma_{xz}$ , respectively, obtained at the same receiver.

We remark that the amplitude of the normal stress component  $\sigma_{xx}$  corresponds to the amplitude of the pressure fluctuations  $p'$  as given in equation 10. Therefore, by using equation 7, we can validate our linearization for the derivation of the wave equations (equation 13) because the maximum of the absolute pressure fluctuation of  $|p'|_{\max} \approx 38.4 \times 10^3$  N/m<sup>2</sup> leads to a maximum density perturbation of  $|\rho'|_{\max} \approx 0.017$  kg/m<sup>3</sup>, which is very small compared with the assumed density of seawater  $\rho = 1020$  kg/m<sup>3</sup>. For completeness, we show the numerical results obtained for the shear stress  $\sigma_{xz}$  in Figure 3. Because water is inviscid ( $\mu = 0$ ), no shear waves appear in the fluid part of the model, which is modeled correctly by the ADER-DG scheme.

In summary, the results confirm the correct implementation of the ADER-DG scheme for the case of fluid-solid interfaces because refracted waves are typically very sensitive to the accurate treatment of material interfaces. We remark that the results shown by Komatitsch et al. (2000) seem to include one more time derivative, most likely caused by the use of the time derivative of a Ricker pulse as source time function.

In summary, the results confirm the correct implementation of the ADER-DG scheme for the case of fluid-solid interfaces because refracted waves are typically very sensitive to the accurate treatment of material interfaces. We remark that the results shown by Komatitsch et al. (2000) seem to include one more time derivative, most likely caused by the use of the time derivative of a Ricker pulse as source time function.

### Source and receiver in the elastic medium

In the second experiment, the source is located at  $\mathbf{x}_s = (x_s, z_s) = (0, 500)$  m and the receiver is located at  $\mathbf{x}_r = (x_r, z_r) = (2177.3, 533.33)$  m, i.e., both below the fluid-solid interface. As pointed out by Komatitsch et al. (2000), with this setup particularly, the correct treatment of the converted P-to-S-wave in the elastic medium can be tested. In Figure 2c and d, we compare three numerical solutions of the horizontal and vertical velocity components of the wavefield with the analytic solution at the new receiver location  $\mathbf{x}_r$ . The agreement of all phases is again excellent, confirming the performance of the high-order ADER-DG O6 scheme and validating the accurate numerical treatment of the fluid-solid interface. As in the previous experiment, the ADER-DG O3 simulations on coarse and fine mesh are less accurate.



### Source and receiver in the moving acoustic medium

In a third experiment, we demonstrate the capability of the ADER-DG method to include a moving fluid. Figure 1 (bottom) shows a similar test to the previous one but with a fluid moving at a speed of 750 m/s to the right. Note that in this case of constant background flow, the reactive source term in equation 15 can be omitted. We observe that the wavelengths of the direct (a) and reflected (b) P-wave in the fluid are strongly distorted because the fluid is moving. In addition, the generated waves (c) and (d) in the elastic medium are moved slightly to the right because, as a result of the moving fluid, the first arrival of the direct P-wave (a) at the fluid-solid interface occurs slightly to the right of the source location  $x = 0$ .

The symmetries of the converted P-to-S-wave (d) and the head waves (e) and (f) are distorted because of the different effective wave-propagation speeds to the right and left in the fluid. In particular, the Scholte wave (g) radiating energy back into the acoustic medium is clearly visible now. The signals are recorded at two receivers at  $\mathbf{x}_l = (-1088.65, -533.33)$  m and  $\mathbf{x}_r = (1088.65, -533.33)$  m, upstream and downstream with respect to source location  $\mathbf{x}_s$ . The locations of the source and receivers are indicated in Figure 1 with empty circles and full squares, respectively. The results are shown in Figure 4.

To visualize the differences, the two rows on the top show the  $u$  and  $w$  components of the signals at the left and right receiver obtained for a fluid at rest overlaid with the analytic reference solution. The two bottom rows show the signals obtained for the moving fluid. We clearly observe the late arrival of the wave phases on the left (upstream) receiver and the early arrival on the right (downstream) receiver. The waveforms are changed because of a different interference of the direct, reflected, and refracted wave phases.

Furthermore, the amplitudes increase on the left and decrease on the right as the energy distribution of the waves in the moving fluid is different; see Figure 1 (bottom). The waves traveling downstream have less amplitude as they are stretched, whereas the waves propagating upstream have increased amplitudes. Note in addition the small velocity amplitudes in Figure 1 compared with the background fluid velocity.

We remark that a fluid velocity of 750 m/s definitely is unrealistically high for marine geophysical applications because the maximum observed velocities of ocean currents are about 2 m/s. However, in exploration seismology, the speed of the seismic vessel has predictable effects on the seismic records (Hampson and Jakubowicz, 1995). A so-called receiver-motion compensation should be used to correct for such effects. Considering techniques such as measurement while drilling (MWD) in borehole applications, the speed of the moving drilling fluid can very well influence the wave-propagation speed of acoustic waves.

Furthermore, many problems in computational aeroacoustics require the accurate simulation of noise propagation in high-speed air flows in which fluid velocity might be of the same order of magnitude as the speed of sound or even higher; see, e.g., Wang et al.

(2006) and Bogey et al. (2002). We remark that the numerical stability condition always takes into account the sum of the fluid velocity and the wave-propagation speed. In the test case presented here, the ratio of the fluid velocity to the acoustic wave speed is 1:2. We further point out that the numerical incorporation of a moving fluid is possible only via formulation of the wave equation as a first-order hyperbolic system, as given in equation 15.

### 3D APPLICATION

To demonstrate the flexibility and potential of the proposed method, we extend the previous 2D numerical experiment to a more realistic and fully 3D test problem of marine seismic exploration. The general procedure to solve problems with complex geometry and rheology is shown schematically in Figure 5. The 3D geometry of the problem is defined by a CAD system and passed to a mesh gener-

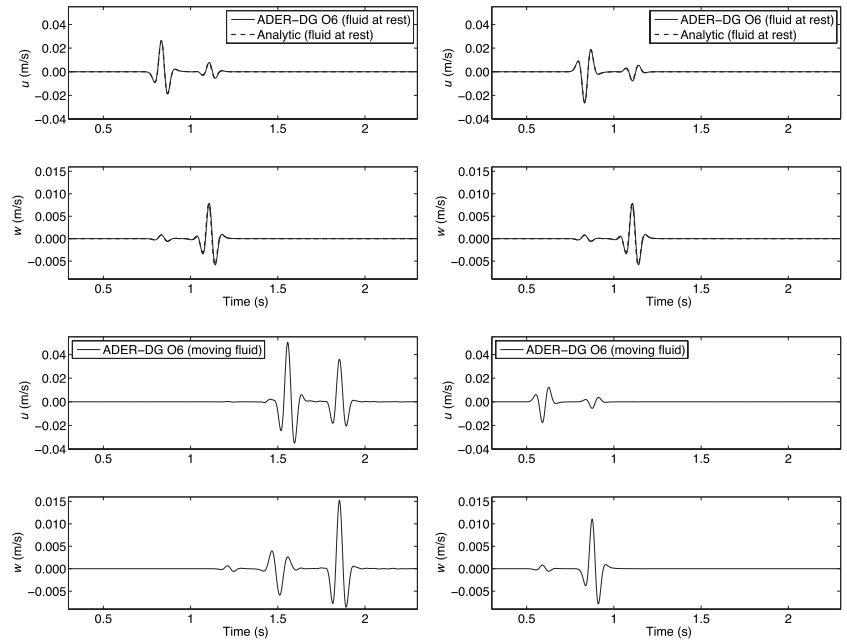


Figure 4. Seismograms for the case of the source and receiver in the acoustic medium. Plots of the left column show the horizontal and vertical velocity components  $u$  and  $w$  for the left receiver  $\mathbf{x}_l = (-1088.65, -533.33)$  and plots of the right column for the right receiver  $\mathbf{x}_r = (1088.65, -533.33)$ . On the top, we show results for the fluid at rest obtained by the ADER-DG O6 scheme (thin solid line) superimposed by the analytic solution (thick dashed line). On the bottom, we show results for the moving fluid obtained by the ADER-DG O6 scheme. Note the delayed arrivals of the wave phases and increased amplitudes at the left receiver and the earlier arrivals and decreased amplitudes on the right receiver, resulting from the background fluid velocity.

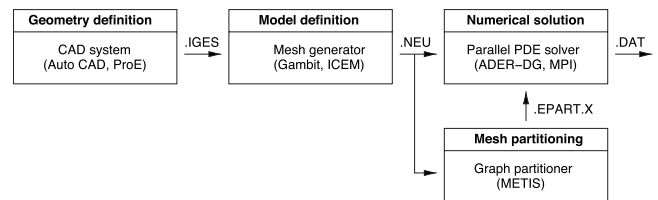


Figure 5. Workflow of the production of synthetic seismograms, including the treatment of arbitrarily complex model geometries and usage of high-performance computer systems.

ator via the IGES standard file format. Afterward, the mesh can be partitioned with the free software package METIS (Karypis and Kumar, 1998) into an arbitrary number of subdomains and imported into the ADER-DG solver using MPI for parallel computations. This procedure is highly optimized and requires few manual interactions.

For the following example, we use tetrahedral elements with plane interfaces, i.e., linear segments defined by vertices. However, we point out that this is not an intrinsic limitation of the ADER-DG

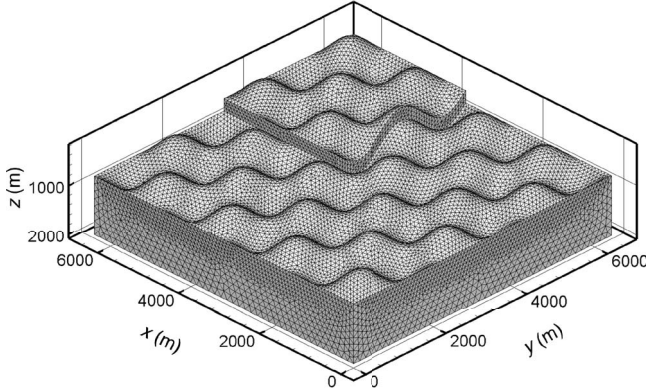


Figure 6. Tetrahedral discretization of the elastic medium with discontinuous sinusoidal ocean-bottom topography. The conforming discretization of the above water layer is not shown so as to make visible the fluid-solid interface with the smooth sinusoidal geometry and the discontinuous step.

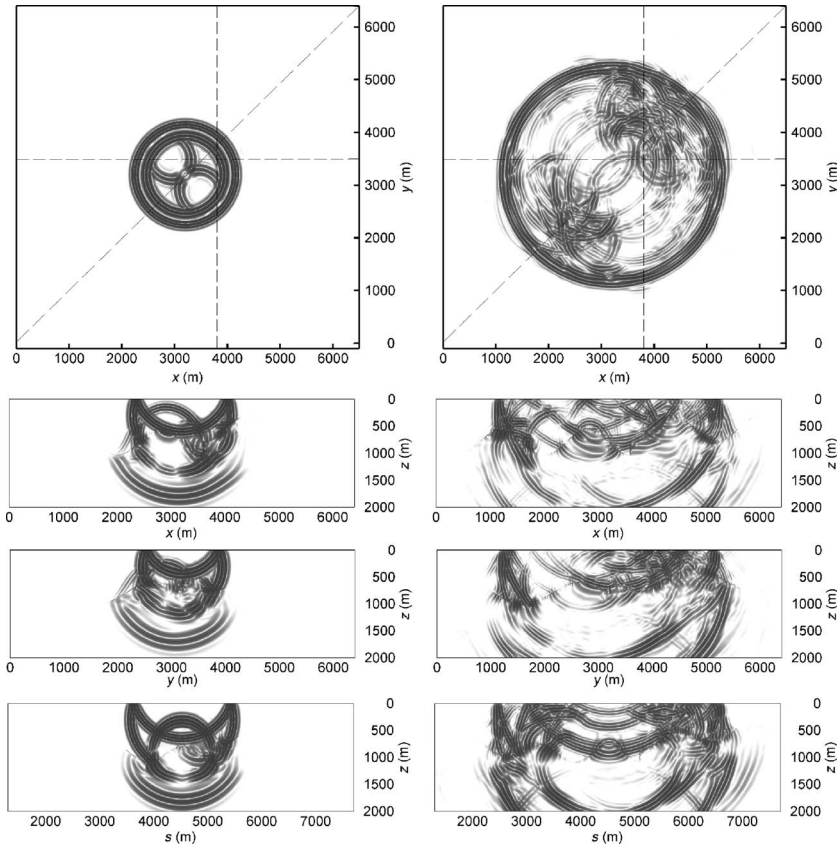


Figure 7. Snapshots of stress component  $\sigma_{zz}$  for the 3D test case at (a)  $t = 0.75$  s and (b)  $t = 1.5$  s in different cutting planes in the  $x$ ,  $y$ , and diagonal directions parameterized by  $s$ .

scheme because superparametric element boundaries also can be used in which the boundaries are represented by high-order polynomials (Dumbser, 2005). We remark that superparametric elements are useful mainly for very coarse meshes when the spatial variation of a boundary is known as an analytic function or as a high-resolution discrete data set. Otherwise, an artificial accuracy of a boundary is introduced, which is not contained in the data set.

The computational domain  $\Omega = [0 \text{ m}, 6400 \text{ m}] \times [0 \text{ m}, 6400 \text{ m}] \times [-2000 \text{ m}, 0 \text{ m}]$  includes a water layer at rest on top of an elastic solid with the fluid-solid interface modeling a complicated bathymetry that has smooth and discontinuous features. The explicit equation for the  $xy$ -dependent elevation  $z$  of the fluid-solid interface is given by

$$z(x, y) = A \cdot \sin(k_x x) \sin(k_y y) - \begin{cases} 550 \text{ m} & \text{for } x > 3600 \text{ m}, y > 3200 \text{ m} \\ 800 \text{ m} & \text{otherwise,} \end{cases} \quad (26)$$

with amplitude  $A = 300 \text{ m}$  and wavenumbers  $k_x = 8/6400\pi \text{ m}^{-1}$  and  $k_y = 6/6400\pi \text{ m}^{-1}$ .

Note that equation 26 represents a sinusoidal interface with a jump, as shown in Figure 6. The model is discretized by 1,993,697 tetrahedral elements of an average edge length of 50 m in the water layer and 100 m in the solid. The minimum edge length of a tetrahedron is 20 m, occurring in the solid material just below the fluid-solid

interface, and the minimum insphere radius  $r^{(m)}$  is 4 m. The water surface at  $z = 0$  is treated as a free-surface boundary, whereas all other domain boundaries are absorbing boundaries. The material parameters are the same as in the 2D examples (see Table 1). The same compressional point source of a 10-Hz Ricker wavelet is used at position  $\mathbf{x}_s = (x_s, y_s, z_s) = (3200, 3200, 300) \text{ m}$ .

Three parallel receiver lines of 101 receivers each are put 2 m below the water surface. Each line starts with the first receiver at  $x = 200 \text{ m}$  and finishes with the last at  $x = 6200 \text{ m}$  with a receiver spacing of 60 m. The  $y$ -coordinates of receivers 1 through 101, 102 through 202, and 203 through 303 are  $y = 1600 \text{ m}$ ,  $y = 3200 \text{ m}$ , and  $y = 4800 \text{ m}$ , respectively. The computation is carried out with an ADER-DG O6 scheme to as high as 2.75 s, leading to  $112 \times 10^6$  degrees of freedom and 27,500 time steps  $\Delta t = 0.1 \text{ ms}$ .

The calculation was performed in 95 hours on an SGI Altix 4700 platform using 255 Intel Itanium2 Madison processors, each with 1.6 GHz and 4 GByte of RAM. At the moment, the computational cost of the ADER-DG method is considerably more expensive than those of many other established methods, as shown in previous work (de la Puente et al., 2007). However, run-time optimization of our implementation is subject to current work.

Snapshots of the stress component  $\sigma_{zz}$  are shown in Figure 7. Snapshots on the top illustrate the wavefield in a horizontal plane at 300-m depth and display the vertical-cut planes of the

subsequent three plots. The first cut is along the  $x$ -direction at  $y = 3500$  m, the next along the  $y$ -direction at  $x = 3800$  m, and the last along the model's diagonal.

In the left column at  $t = 0.75$  s, we observe clearly the reflected wave at the water surface, a strong first reflection from the fluid-solid interface, and the P-to-S converted wave in the solid. Furthermore, the sharp corner of the discontinuity in the ocean bottom acts as a point diffractor, whereas headwaves follow the smoothly varying elevation of the fluid-solid interface. After  $t = 1.5$  s, the wavefield becomes increasingly complex because of the interference of multiple reflections between the water surface and the geometrically complex ocean bottom.

Figure 8 shows the corresponding amplitude-balanced seismograms of  $\sigma_{zz}$  computed at receivers 102 through 202 and 203 through 303. Except for the direct wave and the first reflections, both plots show earlier arrivals of strong reflection signals on the right side of the sections, resulting from the shallower water depth. In addition,

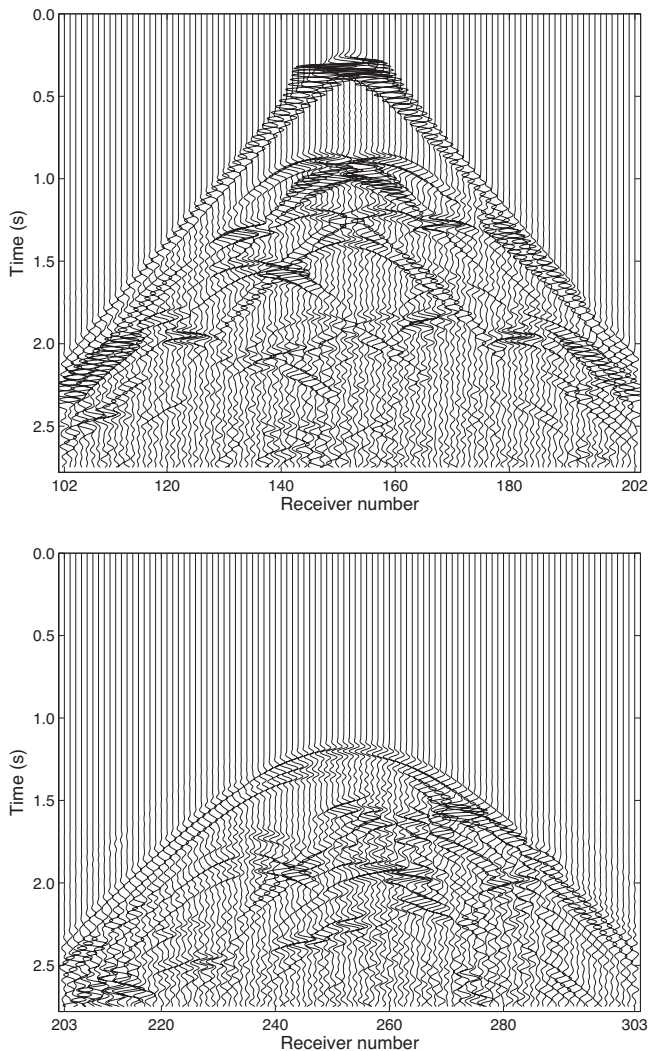


Figure 8. Seismograms of stress component  $\sigma_{zz}$  at (a) the central receiver line ( $y = 3200$  m) with receivers from 102 through 202 and at (b) the laterally shifted receiver line ( $y = 4800$  m) with receivers from 203 through 303. Note the strong multiple reflections and early arrivals of weak signals resulting from head-wave energy radiated into the water layer.

we observe weak signals even before the arrival of the direct wave. These signals are caused by headwaves generated along the fluid-solid interface and radiating energy into the water layer.

We remark that the potential of the new forward-modeling tool ADER-DG lies in the highly accurate synthetic data sets that can be produced for geometrically complex models. These data sets can be used in modern inversion techniques and 3D seismic data-processing algorithms to reveal, with high precision, geometrically complex subsurface structures.

## CONCLUSIONS

We presented the extension of the flexible, highly accurate ADER-DG approach for unstructured 2D and 3D meshes to simulate seismic wave propagation in heterogeneous media containing fluid-solid interfaces. Furthermore, we found that a moving fluid can be considered, when formulating the wave equations as a unified set of first-order hyperbolic equations of motion similar to the classical velocity-stress formulation. This finding allows for a single scheme to be used for the entire domain without a special treatment of internal boundary conditions at strong discontinuities of the material properties.

In particular, the presented extension of the ADER-DG method can be used to accurately model seismic wave propagation in heterogeneous media containing fluid-solid interfaces, including cases in which the fluid has a mean background flow, by simply setting the background flow to zero in the solid and the shear modulus to zero in the fluid. In the case of the moving fluid, the background velocity can be incorporated into the system by simply adding new entries on the diagonal of the Jacobian matrices. Then the exact Riemann solver at the element interfaces automatically treats the fluid-solid interface correctly. In this way, we avoid additional continuity conditions or vanishing shear stress conditions along arbitrarily shaped fluid-solid interfaces.

The ability to represent, simply and accurately, such general situations exceeds the capabilities of the methods now used, e.g., FD or SE methods. Because of the unified formulation and application of the Riemann solver, there is no additional computational cost. However, for nonconstant background flows of strong velocity perturbations, an additional reactive source term must be included. This term increases the computational cost to an extent that depends on the used approximation order of the numerical scheme. We validated the ADER-DG scheme against analytic solutions and conclude that high-order schemes provide a better trade-off of cost versus accuracy than do lower-order schemes on finer meshes.

The main impact of our work on computational seismology is that it allows a new class of problems to be treated in which fluid-solid interfaces are present. In regional or exploration seismology, a water layer with geometrically complex bathymetry now can be included in an analogous manner as real free-surface topography. In this way, the effect of the water layer on the seismic signature, e.g., ghosts or multiples, can be studied accurately.

Therefore, we believe that the extended ADER-DG scheme might become increasingly important as a forward-modeling tool for modern inversion techniques in which highly accurate synthetics are essential to determine the residuals with respect to observations. Furthermore, simulations including a moving fluid might be of interest in cases in which the fluid velocity cannot be neglected, such as time-lapse applications in deep water with strong ocean currents.



## ACKNOWLEDGMENTS

The authors thank the DFG (Deutsche Forschungsgemeinschaft) because the work was supported through the Emmy Noether Programm (KA 2281/1-1), the DFG Forschungsstipendium (DU 1107/1-1), and the DFG-CNRS research group FOR 508, “Noise Generation in Turbulent Flows.” We highly acknowledge the support of Dimitri Komatitsch for providing the analytic solutions and the help of Martin Felder and the Leibniz-Rechenzentrum in München, Germany, for the use of their supercomputing facilities. Furthermore, we thank Peeter Akerberg and the anonymous associate editor and other reviewers for the constructive comments and the interesting and fruitful scientific discussions.

## APPENDIX A

## ORTHOGONAL BASIS FUNCTIONS

We use orthogonal hierarchical basis functions, as given in Cockburn et al. (2000). The basis functions are given in terms of the Jacobian polynomials  $P_n^{\alpha,\beta}(x)$ , which are solutions of the Jacobian differential equation

$$(1 - x^2)y'' + [\beta - \alpha - (\alpha + \beta + 2)x]y' + n(n + \alpha + \beta + 1)y = 0. \quad (\text{A-1})$$

They are given on the interval  $[-1; 1]$  by

$$P_n^{\alpha,\beta}(x) = \frac{(-1)^n}{2^n n!} (1 - x)^{-\alpha} (1 + x)^{-\beta} \frac{d^n}{dx^n} \times [(1 - x)^{\alpha+n} (1 + x)^{\beta+n}]. \quad (\text{A-2})$$

For  $\alpha = \beta = 0$ , the Jacobian polynomials  $P_n^{0,0}(x)$  reduce to the Legendre polynomials.

The discontinuous Galerkin basis functions are constructed then using the three primal functions

$$\begin{aligned} \Theta_i^a(x) &= P_i^{0,0}(x), \quad \Theta_{ij}^b(x) = \left(\frac{1-x}{2}\right)^i P_j^{2i+1,0}(x), \\ \Theta_{ijk}^c(x) &= \left(\frac{1-x}{2}\right)^{i+j} P_k^{2i+2j+2,0}(x). \end{aligned} \quad (\text{A-3})$$

The sets of basis functions  $\Phi_k$  constitute orthogonal basis systems with respect to the inner product on the respective reference elements  $T_E$ .

For tetrahedrons, the reference element  $T_E$  is defined as

$$T_E = \{(\xi, \eta, \zeta) \in \mathbb{R}^3 | 0 \leq \xi \leq 1 \wedge 0 \leq \eta \leq 1 - \xi \wedge 0 \leq \zeta \leq 1 - \xi - \eta\}. \quad (\text{A-4})$$

The basis functions  $\Phi_k(\xi, \eta, \zeta)$  are defined on this reference element as the following product of the primal functions:

$$\Phi_{k(p,q,r)}(\xi, \eta, \zeta) = \Theta_p^a(\alpha) \cdot \Theta_{pq}^b(\beta) \cdot \Theta_{pqr}^c(\gamma), \quad (\text{A-5})$$

with

$$\begin{aligned} \alpha &= \frac{\eta - 1 + \zeta + 2\xi}{1 - \eta - \zeta}, \quad \beta = \frac{2\eta - 1 + \zeta}{1 - \zeta}, \\ \gamma &= -1 + 2\zeta. \end{aligned} \quad (\text{A-6})$$

The monoindex  $k = k(p, q, r)$  is again a function of the index triple  $(p, q, r)$ . The 3D basis functions to as high as degree two for a third-order scheme are

$$\begin{aligned} \Phi_0 &= 1, \\ \Phi_1 &= -1 + 2\xi + \eta + \zeta, \\ \Phi_2 &= -1 + 3\eta + \zeta, \\ \Phi_3 &= -1 + 4\zeta, \\ \Phi_4 &= 1 - 6\xi + 6\xi^2 - 2\eta + 6\xi\eta + \eta^2 - 2\zeta + 6\xi\zeta \\ &\quad + 2\eta\zeta + \zeta^2, \\ \Phi_5 &= 1 - 2\xi - 6\eta + 10\xi\eta + 5\eta^2 - 2\zeta + 2\xi\zeta \\ &\quad + 6\eta\zeta + \zeta^2, \\ \Phi_6 &= 1 - 8\eta + 10\eta^2 - 2\zeta + 8\eta\zeta + \zeta^2, \\ \Phi_7 &= 1 - 2\xi - \eta - 7\zeta + 12\xi\zeta + 6\eta\zeta + 6\zeta^2, \\ \Phi_8 &= 1 - 3\eta - 7\zeta + 18\eta\zeta + 6\zeta^2, \\ \Phi_9 &= 1 - 10\zeta + 15\zeta^2, \end{aligned} \quad (\text{A-7})$$

## REFERENCES

- Berg, P., F. If, P. Nielsen, and O. Skovgaard, 1994, Analytical reference solutions, in K. Helbig, ed., *Modeling the earth for oil exploration*: Pergamon Press.
- Bermudez, A., L. Hervella-Nieto, and R. Rodriguez, 1999, Finite element computation of three-dimensional elastoacoustic vibrations: *Journal of Sound and Vibration*, **219**, 279–306.
- Bogey, C., C. Bailly, and D. Juvé, 2002, Computation of flow noise using source terms in linearized Euler's equations: *AIAA Journal*, **40**, no. 2, 235–243.
- Chaljub, E., Y. Capdeville, and J.-P. Vilotte, 2003, Solving elastodynamics in a fluid-solid heterogeneous sphere: A parallel spectral element approximation on non-conforming grids: *Journal of Computational Physics*, **187**, 457–491.
- Cockburn, B., G. E. Karniadakis, and C. W. Shu, 2000, *Discontinuous Galerkin methods: Lecture notes in computational science and engineering*: Springer.
- Courant, R., K. Friedrichs, and H. Lewy, 1928, Über die partiellen Differenzialgleichungen der mathematischen Physik: *Mathematische Annalen*, **100**, 32–74.
- Cunha, C., 1993, Elastic modeling in discontinuous media: *Geophysics*, **58**, 1840–1851.
- de Hoop, A., 1960, A modification of Cagniard's method for solving seismic pulse problems: *Applied Scientific Research*, **B8**, 349–356.
- de Hoop, A., and J. van der Hijden, 1983, Generation of acoustic waves by an impulsive line source in a fluid/solid configuration with a plane boundary: *Journal of the Acoustical Society of America*, **74**, 333–342.
- de la Puente, J., M. Käser, M. Dumbser, and H. Igel, 2007, An arbitrary high-order discontinuous Galerkin method for elastic waves on unstructured meshes IV: Anisotropy: *Geophysical Journal International*, **169**, 1210–1228.
- Dumbser, M., 2005, *Arbitrary high-order schemes for the solution of hyperbolic conservation laws in complex domains*: Ph.D. thesis, Universität Stuttgart.
- Dumbser, M., and M. Käser, 2006, An arbitrary high-order discontinuous Galerkin method for elastic waves on unstructured meshes II: The three-dimensional case: *Geophysical Journal International*, **167**, 319–336.
- Dumbser, M., M. Käser, and E. Toro, 2007, An arbitrary high-order discontinuous Galerkin method for elastic waves on unstructured meshes V: Local time stepping and  $p$ -adaptivity: *Geophysical Journal International*, **171**, 695–717.

- Hampson, G., and H. Jakubowicz, 1995, The effects of source and receiver motion on seismic data: *Geophysical Prospecting*, **43**, 221–244.
- Hirsch, C., 1990, Numerical computation of internal and external flows, v. 2, Computational methods for inviscid and viscous flows: John Wiley & Sons.
- Karypis, G., and V. Kumar, 1998, Multilevel  $k$ -way partitioning scheme for irregular graphs: *Journal of Parallel and Distributed Computing*, **48**, 96–129.
- Käser, M., and M. Dumbser, 2006, An arbitrary high-order discontinuous Galerkin method for elastic waves on unstructured meshes I: The two-dimensional isotropic case with external source terms: *Geophysical Journal International*, **166**, 855–877.
- Käser, M., M. Dumbser, J. de la Puente, and H. Igel, 2007, An arbitrary high-order discontinuous Galerkin method for elastic waves on unstructured meshes III: Viscoelastic attenuation: *Geophysical Journal International*, **168**, 224–242.
- Kawashima, S., and M. Kimura, 1998, Determination of shear-wave velocity profile using Scholte waves in marine sediments: *Japanese Journal of Applied Physics*, **1**, 3156–3160.
- Kiefling, L., and G. C. Feng, 1976, Fluid-structure finite element vibrational analysis: *AIAA Journal*, **14**, 199–203.
- Komatitsch, D., C. Barnes, and J. Tromp, 2000, Wave propagation near a fluid-solid interface, A spectral-element approach: *Geophysics*, **65**, 623–631.
- Komatitsch, D., and J. Tromp, 1999, Introduction to the spectral-element method for 3-D seismic wave propagation: *Geophysical Journal International*, **139**, 806–822.
- Komatitsch, D., and J. P. Vilotte, 1998, The spectral-element method, An efficient tool to simulate the seismic response of 2D and 3D geological structures: *Bulletin of the Seismological Society of America*, **88**, 368–392.
- Landau, L. D., and E. M. Lifshitz, 1959, Fluid mechanics: Pergamon Press.
- LeVeque, R., 2002, Finite volume methods for hyperbolic problems: Cambridge University Press.
- Moczo, P., J. Kristek, M. Galis, P. Pazak, and M. Balazovjeh, 2007a, The finite-difference and finite-element modeling of seismic wave propagation and earthquake motion: *Acta physica slovacica*, **57**, 177–406.
- Moczo, P., J. Kristek, V. Vavrycuk, R. J. Archuleta, and L. Halada, 2002, 3D heterogeneous staggered-grid finite-difference modeling of seismic motion with volume harmonic and arithmetic averaging of elastic moduli and densities: *Bulletin of the Seismological Society of America*, **92**, 3042–3066.
- Moczo, P., J. O. A. Robertsson, and L. Eisner, 2007b, The finite-difference time domain method for modeling of seismic wave propagation, in R.-S. Wu, and V. Maupin, eds., *Advances in wave propagation in heterogeneous earth*, Elsevier Science, *Advances in Geophysics* 48, 421–516.
- Munz, C., M. Dumbser, and S. Roller, 2007, Linearized acoustic perturbation equations for low mach number flow with variable density and temperature: *Journal of Computational Physics*, **224**, 352–364.
- Pilant, W. L., 1979, Elastic waves in the earth: Elsevier Science.
- Priolo, E., J. M. Carcione, and G. Seriani, 1994, Numerical simulation of interface waves by high-order spectral modeling techniques: *Journal of the Acoustical Society of America*, **95**, 681–693.
- Robertsson, J. O. A., 1996, A numerical free-surface condition for elastic/viscoelastic finite-difference modeling in the presence of topography: *Geophysics*, **61**, 1921–1934.
- Scholte, J., 1942, On the Stoneley wave equation: *Proceedings of the Koninklijke Nederlandse Akademie van Wetenschappen*, **45**, 20–25 159–164.
- Seriani, G., E. Priolo, J. Carcione, and E. Padovani, 1992, High-order spectral element method for elastic wave modeling: 62nd Annual International Meeting and Exposition, SEG Expanded Abstracts, 1285–1288.
- Thompson, L. L., 1994, Design and analysis of space-time and Galerkin-least-squares finite element methods for fluid-structure interactions in exterior domains: Ph.D. thesis, Stanford University.
- Toro, E. F., 1999, Riemann solvers and numerical methods for fluid dynamics: Springer.
- van Vossen, R., J. Robertsson, and C. Chapman, 2002, Finite-difference modeling of wave propagation in a fluid-solid configuration: *Geophysics*, **67**, 618–624.
- Wang, M., J. Freund, and S. Lele, 2006, Computational prediction of flow-generated sound: *Annual Review of Fluid Mechanics*, **38**, 483–512.
- Zahradník, J., P. Moczo, and F. Hron, 1993, Testing four elastic finite-difference schemes for behaviour at discontinuities: *Bulletin of the Seismological Society of America*, **83**, 107–129.
- Zhang, J., 2004, Wave propagation across fluid-solid interfaces: A grid method approach: *Geophysical Journal International*, **159**, 240–252.
- Zienkiewicz, O. C., and P. Bettess, 1978, Fluid-structure dynamic interaction and wave forces: An introduction to numerical treatment: *International Journal for Numerical Methods in Engineering*, **13**, 1–16.